Article | Open Access

Energy Materials

Huang *et al. Energy Mater.* **2026**, *6*, 600158 **DOI:**10.20517/energymater.2026.252

Electronically active Sn nanosheets enable Sn-to-Pt interfacial charge redistribution for acidic and alkaline hydrogen evolution

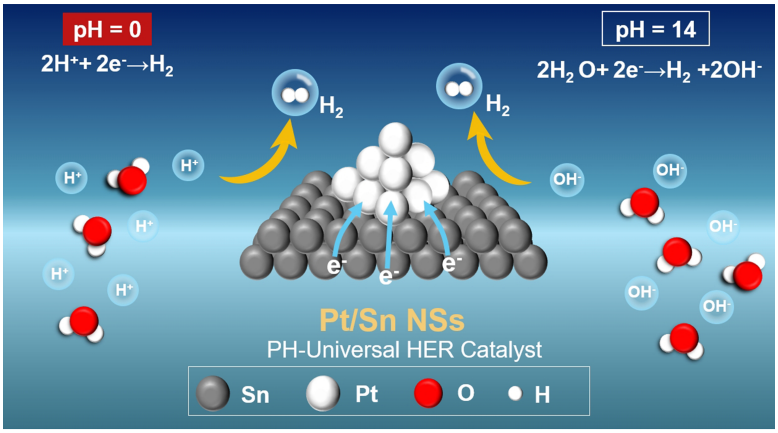
Yifan Huang[1,#], Hailin Jiao[2,#], Bowen Bai[1,*], Lin Zhao[1], Li Liu[3,4], Tao Yu[1], Futang Li[1], Min Zhao[2], Jingkun Wang[2], Quan Bai[1], Jin Li[1,*], Xuesong Leng[1,*]

Keywords:
Hydrogen evolution reaction, Pt-support electronic coupling, Sn nanosheets, d-band modulation, electrocatalysis

Citation: Huang, Y.; Jiao, H.; Bai, B.; Zhao, L.; Liu, L.; Yu, T.; Li, F.; Zhao, M.; Wang, J.; Bai, Q.; Li, J.; Leng, X. Electronically active Sn nanosheets enable Sn-to-Pt interfacial charge redistribution for acidic and alkaline hydrogen evolution. *Energy Mater.* **2026**, *6*, 600158. https://dx.doi.org/10.20517/energymater.2026.252

Received: 30 Jul 2026
First Decision: 20 Aug 2026
Revised: 9 Oct 2026
Accepted: 15 Oct 2026
Published: 17 Nov 2026

Academic Editor:
Ho Won Jang
Copy Editor:
Ping Zhang
Production Editor:
Ping Zhang



Abstract

Regulating Pt-support electronic coupling is crucial for improving the activity, durability, and Pt utilization of hydrogen evolution reaction (HER) electrocatalysts. However, the weak electronic interaction between Pt nanoparticles and conventional carbon supports in commercial platinum-on-carbon (Pt/C) limits further performance enhancement. Herein, we report a two-dimensional Sn nanosheet-supported Pt nanoparticle catalyst (Pt/Sn NSs) constructed by liquid-phase exfoliation and atomic layer deposition. Structural and surface chemical analyses reveal pronounced interfacial electronic coupling between Pt nanoparticles and the Sn-based support. Combined with density functional theory calculations, the results demonstrate Sn-to-Pt interfacial charge redistribution and enhanced Pt stabilization on Sn nanosheets. Benefiting from this strengthened Pt-support electronic interaction, Pt/Sn NSs exhibit superior HER performance compared to commercial Pt/C in both acidic and alkaline media, requiring only 28 mV in 0.5 M H_2SO_4

[1]Research Institute of Physical Sciences in Special Environments, Harbin Institute of Technology (Shenzhen), Shenzhen 518055, Guangdong, China.
[2]College of Physics and Optoelectronics, Shanxi Key Lab of Photovoltaic Technology and Application, Key Lab of Advanced Transducers and Intelligent Control System, Ministry of Education, Taiyuan University of Technology, Taiyuan 030024, Shanxi, China.
[3]School of Materials Science and Engineering, Harbin Institute of Technology (Shenzhen), Shenzhen 518055, Guangdong, China.
[4]National Key Laboratory of Precision Hot Processing of Metals, Harbin Institute of Technology, Harbin 150001, Heilongjiang, China.
[#]These authors contributed equally to this work.

[*]**Correspondence to:** Dr. Bowen Bai, Dr. Jin Li, Dr. Xuesong Leng, Research Institute of Physical Sciences in Special Environments, Harbin Institute of Technology (Shenzhen), Shenzhen 518055, Guangdong, China. E-mail: baibowen@hit.edu.cn; lijin2019@hit.edu.cn; lengxuesong@hit.edu.cn

and 37 mV in 1.0 M KOH to reach 10 mA cm^{-2}, with Tafel slopes of 13.5 and 35.7 mV dec^{-1}, respectively. The calculations further show support-induced modulation of the Pt electronic structure, a more nearly thermoneutral H* adsorption state, and more favorable reaction thermodynamics for the key HER steps. This work demonstrates that electronically interactive Sn nanosheets provide an effective support-engineering platform for regulating Pt-based HER electrocatalysis.

INTRODUCTION

Hydrogen production through electrocatalytic water splitting has been regarded as one of the most promising routes for sustainable energy conversion because it enables the generation of high-purity hydrogen using renewable electricity[1-3]. As the cathodic half-reaction of water electrolysis, the hydrogen evolution reaction (HER) requires efficient electrocatalysts to lower the reaction overpotential and accelerate interfacial charge-transfer kinetics[2-5]. To date, Pt-based catalysts remain the benchmark for HER owing to their near-optimal hydrogen adsorption free energy, low overpotential, and high exchange current density[4-7]. However, the scarcity and high cost of Pt severely restrict its large-scale application. More importantly, Pt nanoparticles are prone to migration, aggregation, detachment, or dissolution during synthesis and long-term electrocatalysis, leading to decreased Pt utilization and catalytic durability[6-10]. Therefore, developing Pt-based electrocatalysts with high Pt utilization efficiency, strong interfacial stability, and enhanced intrinsic activity remains a central challenge for efficient hydrogen production.

Electronic metal-support interaction (EMSI) has emerged as an effective strategy for regulating the activity, stability, and noble-metal utilization of supported electrocatalysts[11-16]. Unlike a passive physical support, an electronically interactive support can induce interfacial charge redistribution and orbital coupling with supported metal species, thereby modifying the electronic structure and adsorption properties of catalytic sites. Strong interfacial interaction may contribute to improved structural stability by strengthening coupling between supported metal species and the substrate[11-16]. More broadly, recent HER studies based on doped carbon, transition-metal chalcogenides, phosphides, oxides, and low-dimensional heterostructures show that interfacial charge transfer, hydrogen spillover, water activation, and site stabilization are effective mechanisms for promoting reaction kinetics[17-27]. These considerations indicate that the support should be regarded as an active component that governs the electronic configuration, interfacial stability, and reaction kinetics of supported Pt catalysts.

Commercial platinum-on-carbon (Pt/C) is currently the most widely used benchmark catalyst for HER because carbon black provides good electrical conductivity, high surface area, and accessible mass-transfer channels for Pt nanoparticle dispersion[8-10,26,27]. However, the relatively inert surface chemistry of pristine carbon generally leads to weak metal-support coupling, which may cause Pt migration, Ostwald ripening, nanoparticle detachment, and active-surface loss during electrocatalysis, ultimately limiting Pt utilization and durability[10,15,26,27]. In this regard, two-dimensional Sn nanosheets are expected to be more suitable supports for constructing strongly coupled Pt-based catalysts. Recent Pt/support and Sn-containing interfacial systems demonstrate that support chemistry can markedly alter charge redistribution and catalytic behavior[28,29], while stanene-based heterostructures further illustrate the capacity of two-dimensional Sn-containing phases to participate in directional interfacial electron transport[30]. According to the Pauling electronegativity scale, Sn (1.96) possesses a lower electronegativity than C (2.55), suggesting a stronger electron-donating tendency and a greater possibility of interfacial electron transfer toward Pt[31]. Such Pt-Sn electronic interaction can induce pronounced charge redistribution, modulate the electron density and d-band structure of Pt active sites, and thereby regulate the adsorption/desorption energetics of hydrogen-related intermediates. In addition, the ultrathin Sn nanosheets expose abundant surface atoms and undercoordinated sites, which can provide plentiful anchoring positions for Pt nucleation, enhance Pt dispersion, shorten electron-transfer

pathways, and create abundant Pt-Sn interfacial sites. Therefore, Sn nanosheets are not merely alternatives to carbon supports, but can also serve as electronically active supports to strengthen Pt-support interaction and promote HER kinetics beyond commercial Pt/C.

Recent studies have demonstrated that the catalytic behavior of Pt can be effectively regulated through support engineering, Pt-Sn compound formation, and multicomponent alloying. For example, Wu *et al.* constructed subnanometer Pt clusters on oxygen-vacancy-rich black TiO_2, where defect-mediated Pt-support interactions promoted acidic HER kinetics[32]. Weng and Alexandrova investigated $PtSn_4$ as a Pt-Sn intermetallic electrocatalyst and revealed that surface reconstruction and the evolution of conducting surface states play important roles in its HER behavior[33]. In another strategy, Yu *et al.* developed IrPdPtRhRu high-entropy alloy nanoparticles with excellent HER activity over a wide pH range[34]. Related Pt-Sn intermetallic heterostructures have also demonstrated pH-universal HER activity through cooperative Pt-Sn/Co interfacial regulation[35]. Very recently, reactive Pt-SnO_2 interfaces were shown to evolve into Pt-Sn intermetallic phases whose structure strongly influences HER activity[36]. These studies highlight the effectiveness of defect engineering, Pt-Sn electronic interactions, and multielement compositional regulation for improving hydrogen electrocatalysis. Nevertheless, oxide-supported Pt catalysts primarily rely on defect-rich oxide interfaces, $PtSn_4$ represents an intrinsically alloyed/intermetallic catalytic phase rather than a supported Pt architecture, and high-entropy alloys require compositionally complex multimetal systems. Therefore, the use of a two-dimensional metallic Sn nanosheet as an electronically active support to regulate the dispersion, anchoring, and electronic structure of Pt nanoparticles, while directly distinguishing the support effect from the conventional Pt/C system under both acidic and alkaline conditions, remains insufficiently explored.

Here, we construct Pt nanoparticle-modified Sn nanosheets (Pt/Sn NSs) by combining liquid-phase exfoliation with atomic layer deposition (ALD). Unlike conventional carbon supports, the two-dimensional Sn nanosheets are designed to function as electronically active supports that provide abundant anchoring sites for ultrasmall Pt nanoparticles and induce pronounced Pt-Sn interfacial electronic coupling. By systematically comparing Pt/Sn NSs with commercial Pt/C, we clarify how the Sn nanosheet support influences Pt dispersion, interfacial charge redistribution, adsorption thermodynamics, Pt utilization, and HER kinetics under both acidic and alkaline conditions. This support-centered design provides a distinct route for regulating supported Pt catalysts without relying on compositionally complex multimetallic architectures.

EXPERIMENTAL

Synthesis of Sn NSs

Two-dimensional tin nanosheets were synthesized by a low-temperature liquid-phase exfoliation under ice-bath conditions. Briefly, tin powder was first ground in an agate mortar for 30 min and then transferred into 100 mL of N,N-dimethylformamide (DMF). The resulting dispersion was subjected to probe ultrasonication in an ice bath at 500 W in a pulsed mode with a pulse duration of 2 s for a total sonication time of 6 h. After ultrasonication, the dispersion was centrifuged at 3,000 rpm for 5 min to remove unexfoliated bulk Sn. The supernatant was collected and further centrifuged at 11,000 rpm for 10 min. The resulting Sn NSs were finally redispersed in DMF for subsequent Pt nanoparticle deposition. The centrifugation steps were performed using a high-speed centrifuge (TGL-15B, Shanghai Anting Scientific Instrument Factory, China).

Preparation of Pt/Sn NSs

The Pt/Sn NSs heterostructure was prepared using ALD (D100-4882, Chongqing Nuotu Technology Co., Ltd., China). Here, 15 mg of Sn NSs were uniformly dispersed on a heat-resistant quartz glass substrate with anhydrous ethanol and then allowed to dry at room temperature. The dried sample was then transferred into the ALD chamber for Pt deposition.

During ALD, the chamber temperature was maintained at 250 °C. Trimethyl(methylcyclopentadienyl)platinum was used as the Pt precursor and heated to 65 °C, with N_2 used as the carrier and purge gas. Each ALD cycle consisted of Pt precursor exposure, reaction, purge, oxidant exposure, reaction, and purge steps. The Pt/Sn NS catalyst used for subsequent experiments was obtained after 60 ALD cycles. After deposition, the material was scraped from the quartz substrate and collected for further characterization and electrochemical measurements. To optimize the Pt loading, Pt/Sn NS samples with different ALD cycles were also prepared.

Material characterization

The surface morphology of the samples was examined by scanning electron microscopy (SEM, JSM-6700, JEOL Ltd., Japan), and the spatial distributions of the constituent elements were analyzed by energy-dispersive X-ray spectroscopy (EDS). The microscopic morphology, lattice structure, and local structural characteristics were further characterized by transmission electron microscopy (TEM, JEM-F200, JEOL Ltd., Japan) operated at an accelerating voltage of 200 kV. The crystalline structure and phase composition were analyzed by X-ray diffraction (XRD, Y-2000, Dandong Aolong Radiative Instrument Co., Ltd., China). The surface elemental composition and chemical states were characterized by X-ray photoelectron spectroscopy (XPS, ESCALAB 250 Xi, Thermo Fisher Scientific, United Kingdom). The Pt content in Pt/Sn NSs was quantitatively determined by inductively coupled plasma optical emission spectroscopy (ICP-OES, Agilent 5110, Agilent Technologies, USA), giving a Pt mass fraction of 13.6 wt%.

Electrochemical measurements

All electrochemical measurements were performed using an electrochemical workstation (CHI 760E, Shanghai Chenhua Instrument Co., Ltd., China). Catalyst inks were homogenized using an ultrasonic cleaner (K3200DE, Kunshan Ultrasonic Instruments Co., Ltd., China). Detailed electrochemical procedures are provided in the Supplementary Materials.

RESULTS AND DISCUSSION

Structural characterization

The synthetic route of Pt/Sn NSs is shown in Figure 1A. Two-dimensional Sn nanosheets were first prepared through an ice-bath-assisted liquid-phase ultrasonication of Sn powder in DMF. Subsequently, Pt nanoparticles were deposited in situ onto the surface of the obtained Sn NSs by ALD at 250 °C without the addition of any solution-phase reducing agents. Pt species can be uniformly nucleated and anchored on the Sn NSs surface due to the self-limiting surface reaction of ALD and the abundant surface sites of the two-dimensional Sn NSs. This synthetic strategy enables the controlled construction of ultrasmall Pt nanoparticles on Sn NSs, forming a 0D/2D Pt/Sn NSs heterostructure with intimate interfacial contact. Such a structure is expected to facilitate Pt dispersion, enhance Pt utilization, and promote strong interfacial coupling between Pt nanoparticles and the Sn nanosheet support. The controllable nucleation and size regulation of supported Pt species by ALD have also been demonstrated in previous studies[37].

The morphology and microstructure of the as-prepared Pt/Sn NSs were first investigated by TEM, high-resolution TEM, SEM, and elemental mapping. As shown in Figure 1B, the pristine Sn NSs exhibit a typical two-dimensional nanosheet morphology with a lateral size of approximately 1 μm, confirming the successful preparation of Sn-based nanosheets. After Pt deposition, numerous nanoparticles are clearly observed on the Sn NSs surface [Figure 1C], and no obvious aggregation can be found, indicating the uniform nucleation and dispersion of Pt nanoparticles on the two-dimensional Sn support. To further identify the crystal structure of the deposited nanoparticles, the region marked by the orange dashed square in Figure 1C was analyzed using an inverse fast Fourier transform. The corresponding lattice-resolved image in Figure 1D shows distinct lattice fringes with an interplanar spacing of 0.23 nm, which can be assigned to the (111) plane of

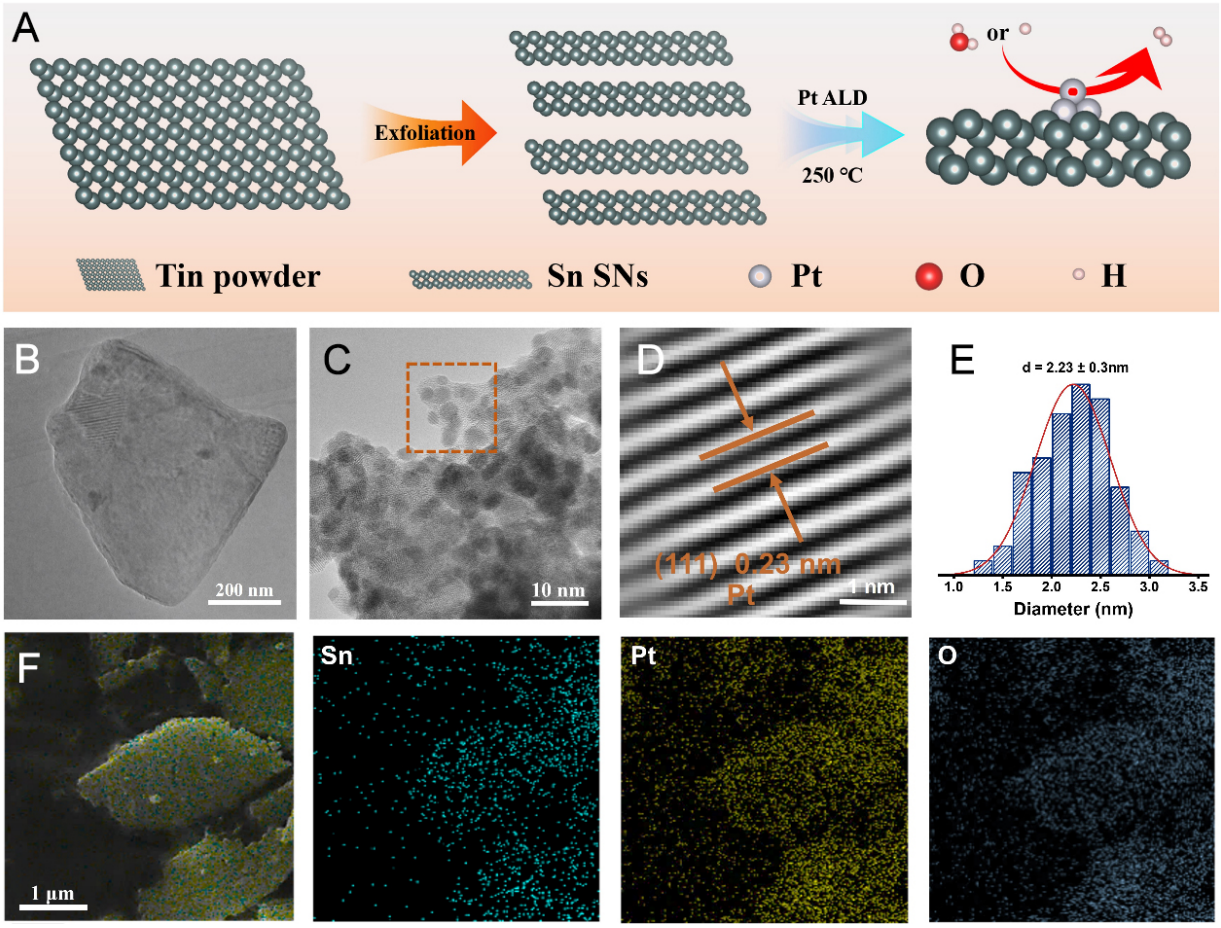


Figure 1. Synthesis and structural characterization of Pt/Sn NSs. (A) Schematic of the fabrication process of Pt/Sn NSs; (B) TEM image of the Sn NSs; (C) TEM image of the Pt/Sn NSs; (D) Enlarged lattice-resolved image taken from the marked region in (C); (E) Particle size distribution of Pt nanoparticles; (F) SEM image and corresponding elemental mappings of Pt/Sn NSs. Pt/Sn NSs: Pt nanoparticle-modified Sn nanosheets; TEM: transmission electron microscopy; SEM: scanning electron microscopy; EDS: energy-dispersive X-ray spectroscopy; ALD: atomic layer deposition.

face-centered cubic Pt, confirming the formation of crystalline metallic Pt nanoparticles. The particle-size distribution histogram in Figure 1E reveals that the Pt nanoparticles possess an average diameter of approximately 2.23 nm, suggesting that ultrasmall Pt nanoparticles were successfully anchored on the Sn NSs surface. ICP-OES analysis further confirmed that the actual Pt content in Pt/Sn NSs is 13.6 wt% [Supplementary Table 1]. The SEM image and corresponding EDS elemental mapping images in Figure 1F further show that the nanosheet morphology is well retained after Pt deposition, with Sn, Pt, and O elements uniformly distributed throughout the nanosheet region. These results collectively confirm the successful construction of a 0D/2D Pt/Sn NSs heterostructure consisting of ultrasmall Pt nanoparticles uniformly distributed on two-dimensional Sn nanosheets with intimate interfacial contact.

The crystal structure of the Pt/Sn NSs was characterized using XRD [Figure 2A]. The diffraction peaks located at 39.72°, 46.18°, 67.66°, and 81.19° can be indexed to the (111), (200), (220), and (311) planes of face-centered cubic Pt, respectively, consistent with JCPDS PDF No. 87-0640. This result confirms that Pt species were successfully deposited onto the Sn NSs surface through ALD and formed crystalline Pt nanoparticles. Meanwhile, the characteristic diffraction peaks of Sn NSs are still retained after Pt deposition, suggesting that the main crystalline structure of Sn NSs was largely preserved during the ALD process. The XRD pattern of pristine Sn NSs [Supplementary Figure 1] further verifies the crystalline phase of the Sn nanosheet support,

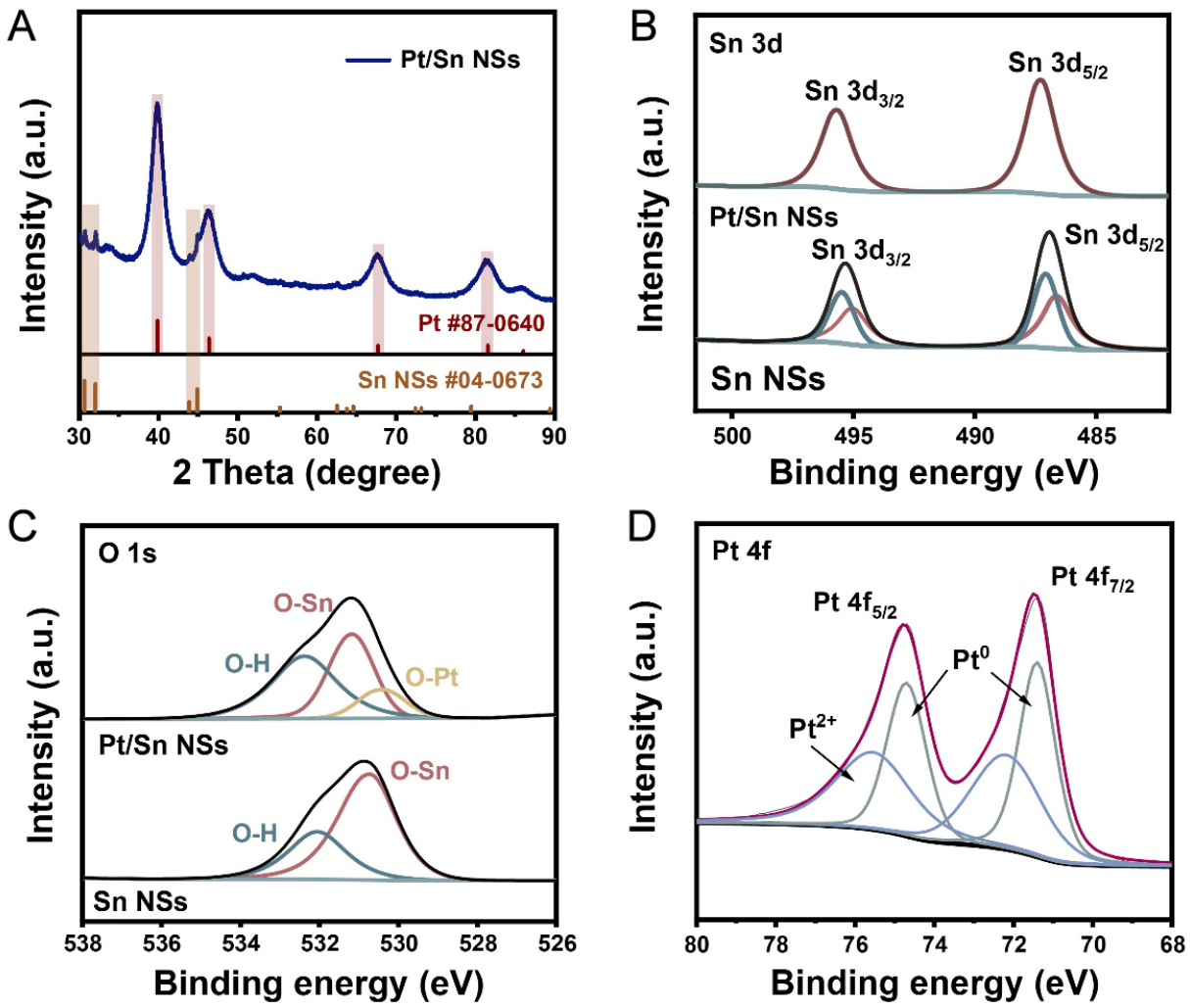


Figure 2. Phase composition and surface chemical-state characterization of Pt/Sn NSs. (A) XRD patterns of the Pt/Sn NSs; (B) High-resolution Sn 3d XPS spectra of the Sn NSs and Pt/Sn NSs; (C) High-resolution O 1s XPS spectra of the Sn NSs and Pt/Sn NSs; (D) High-resolution Pt 4f XPS spectrum of the Pt/Sn NSs. Pt/Sn NSs: Pt nanoparticle-modified Sn nanosheets; XRD: X-ray diffraction; XPS: X-ray photoelectron spectroscopy.

providing a reliable reference for identifying the retained Sn-related diffraction features in Pt/Sn NSs. Combined with the aforementioned TEM results, these phase-structure analyses demonstrate that crystalline Pt nanoparticles were successfully anchored on the surface of the two-dimensional Sn NSs, forming a 0D/2D Pt/Sn NSs heterostructure.

The surface elemental composition and binding states of Pt/Sn NSs, particularly the interfacial charge redistribution and chemical environment, were examined using XPS. The survey XPS spectrum of the Pt/Sn NSs [Supplementary Figure 2] confirms the presence of Pt, Sn, and O, consistent with the elemental mapping results. The high-resolution Sn 3d spectra are shown in Figure 2B. For the pristine Sn NSs, the peaks at 486.6/495.1 eV and 487.1/495.5 eV can be assigned to Sn^{2+} and Sn^{4+} species, respectively[38]. After Pt deposition, the Sn 3d peaks shift toward higher binding energies, suggesting a decrease in the electron density around Sn and the occurrence of interfacial charge redistribution between the Pt nanoparticles and the Sn-based support[39,40]. These changes are consistent with Pt-Sn interfacial electronic coupling, while XPS results alone are insufficient to establish a specific classical strong metal-support interaction structure.

The O 1s spectra provide further evidence for interfacial chemical coupling. As illustrated in Figure 2C, the O 1s spectrum of Sn NSs can be fitted into O-Sn and O-H components, corresponding to surface tin oxide species and hydroxyl/adsorbed oxygen-containing species, respectively[38]. After Pt deposition, an additional O-Pt-related component is observed in Pt/Sn NSs. The coexistence of O-Sn and O-Pt surface species is consistent with the presence of oxygen-containing surface species associated with the Pt/Sn interface[6,39,41]. Figure 2D shows the high-resolution Pt 4f spectrum of the Pt/Sn NSs. The peaks at 71.5 and 74.8 eV are assigned to Pt^0 $4f_{7/2}$ and Pt^0 $4f_{5/2}$, confirming metallic Pt nanoparticles on the Sn NSs surface, while the Pt^{2+} components at higher binding energies are associated with Pt-O-related surface species[29,40,42]. Together, the Sn 3d, O 1s, and Pt 4f results support a chemically and electronically coupled Pt/Sn interface rather than simple physical deposition of Pt nanoparticles on the Sn NSs.

Electrochemical performance of HER

To determine the optimal Pt loading on the Sn NSs, the HER activities of Pt/Sn NSs with different ALD deposition cycles were first evaluated in 0.5 M H_2SO_4. Supplementary Figure 3 shows that the catalytic activity exhibits an obvious dependence on the number of ALD cycles. When the number of deposition cycles increases from 40 to 60, the overpotential required to reach 10 mA cm^{-2} gradually decreases from 40 to 28 mV, indicating that increasing the Pt deposition amount can provide more accessible Pt active sites and improve the HER activity[37,43]. However, further increasing the number of deposition cycles to 70 leads to an increased overpotential of 42 mV, suggesting that excessive Pt deposition may reduce the effective utilization of Pt species and limit the contribution of Pt-Sn interfacial regions[7,42,43]. Therefore, Pt/Sn NSs with 60 ALD cycles were selected as the optimized catalyst for the following electrochemical measurements.

The HER performances of Pt/Sn NSs and representative reported catalysts in acidic and alkaline media are summarized in Supplementary Tables 2 and 3, respectively. The HER performance of the optimized Pt/Sn NSs was first evaluated in 0.5 M H_2SO_4. As shown in Figure 3A, the Pt/Sn NSs exhibit superior acidic HER activity compared with commercial Pt/C, requiring only 28 and 46 mV to reach current densities of 10 and 100 mA cm^{-2}, respectively, whereas Pt/C requires 34 and 155 mV at the same current densities. The corresponding overpotential comparison in Figure 3B further confirms the enhanced HER activity of Pt/Sn NSs. As shown in Figure 3C, Pt/Sn NSs exhibit an apparent Tafel slope of 13.5 mV dec^{-1}, substantially smaller than that of commercial Pt/C. The corresponding current-density fitting ranges and linear regression parameters are summarized in Supplementary Table 4, and the fitted-line coordinates for the acidic electrolyte are provided in Supplementary Table 5. Under the idealized classical Volmer-Heyrovsky-Tafel framework, slopes of approximately 120, 40, and 30 mV dec^{-1} are commonly associated with Volmer-, Heyrovsky-, and Tafel-limited kinetic regimes, respectively[44]. These characteristic values depend on the assumptions of the idealized model; therefore, approximately 30 mV dec^{-1} should not be treated as an absolute lower bound for a slope fitted from an experimental polarization curve. In particular, the measured net current and the intrinsic rate of an individual HER elementary step are not necessarily equivalent. Kinetic modeling of Pt-based HER has shown that a contribution from the reverse hydrogen oxidation reaction near equilibrium can, in a simplified case, yield a fitted apparent slope near 15 mV dec^{-1} even when the underlying HER slope is 30 mV dec^{-1}[44]. This provides a physically grounded example of how a value below 30 mV dec^{-1} can arise, and it does not establish that hydrogen reoxidation is the origin of the present 13.5 mV dec^{-1} value. Similarly low apparent slopes have been reported for Pt/CNT_{45} (~17 mV dec^{-1}), $Pt_{56}Fe_{44}$ (~22 mV dec^{-1}), and Pt_3Co@NCNT (~27.2 mV dec^{-1}), as summarized in Supplementary Table 2. Accordingly, we use 13.5 mV dec^{-1} as an apparent kinetic descriptor under the present measurement conditions and do not assign a unique rate-determining step or a specific microscopic origin from this slope alone.

The mass activities were evaluated at a geometric current density of 10 mA cm^{-2} in the respective electrolytes by normalizing the corresponding current to the mass of Pt loaded on each working electrode. As shown in Supplementary Figure 4, the Pt/Sn NSs exhibit a mass activity of 103.38 A $mgPt^{-1}$ in 0.5 M H_2SO_4, which far

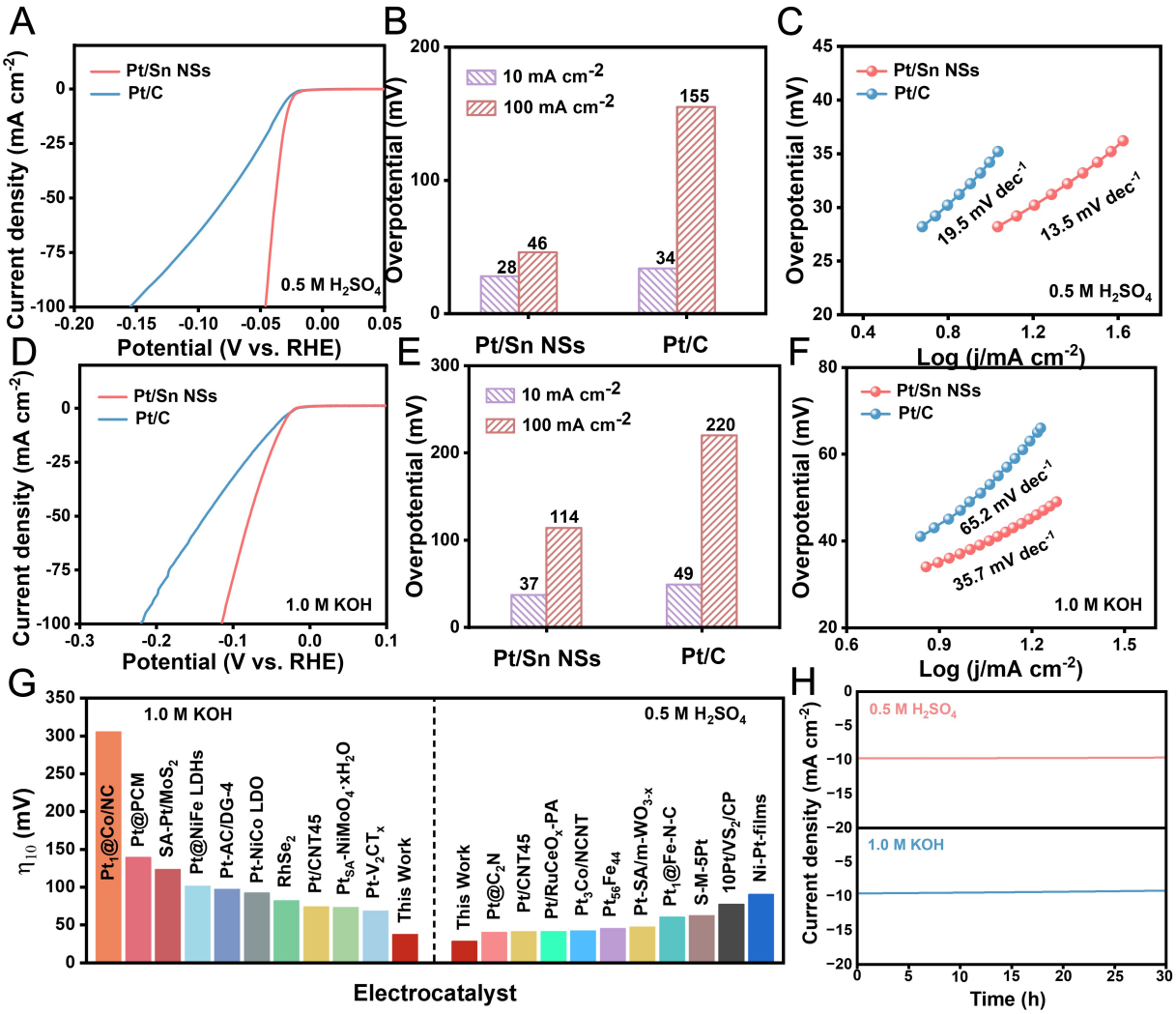


Figure 3. HER performance of Pt/Sn NSs and commercial 20 wt% Pt/C in acidic and alkaline electrolytes. (A-C) LSV polarization curves, overpotential comparison at current densities of 10 and 100 mA cm^{-2}, and corresponding Tafel plots in 0.5 M H_2SO_4, respectively; (D-F) LSV polarization curves, overpotential comparison at current densities of 10 and 100 mA cm^{-2}, and corresponding Tafel plots in 1.0 M KOH, respectively. In (A), (C), (D), and (F), the red and blue curves represent Pt/Sn NSs and commercial 20 wt% Pt/C, respectively; (G) Comparison of the HER performance of the Pt/Sn NSs with recently reported HER electrocatalysts in acidic and alkaline media; (H) Long-term chronoamperometric durability curves of the Pt/Sn NSs measured for 30 h under constant applied potentials in 0.5 M H_2SO_4 and 1.0 M KOH. The red and blue curves in (H) correspond to the Pt/Sn NSs measured in 0.5 M H_2SO_4 and 1.0 M KOH, respectively. Pt/Sn NSs: Pt nanoparticle-modified Sn nanosheets; HER: hydrogen evolution reaction; Pt/C: platinum-on-carbon; LSV: linear sweep voltammetry; RHE: reversible hydrogen electrode.

exceeds that of commercial Pt/C (15.3 A $mgPt^{-1}$). This result demonstrates that the Pt nanoparticles anchored on the Sn NSs possess significantly elevated Pt utilization efficiency[5,6]. The enhanced mass activity can be attributed to the ultrasmall Pt nanoparticles, their uniform dispersion on the two-dimensional Sn support, and the abundant Pt-Sn interfacial sites[15,45,46]. The intrinsic activity of the active sites was further assessed by turnover frequency (TOF) analysis. As illustrated in Supplementary Figure 5, the Pt/Sn NSs display much higher TOF values than Pt/C over the tested overpotential range, and the difference becomes pronounced with increasing overpotential. This indicates that the Pt active sites in Pt/Sn NSs possess higher apparent intrinsic activity under the tested conditions, further confirming that Sn NSs serve not only as a physical support but also as an electronically active support to regulate the catalytic behavior of Pt nanoparticles[11,15,45,46].

To assess the relative electrochemically accessible surface area, cyclic voltammetry (CV) measurements were performed in the non-Faradaic region [Supplementary Figure 6] to determine the electrochemical double-layer capacitance (Cdl). Supplementary Figure 7 shows that Pt/Sn NSs exhibit larger capacitive currents than Pt/C at different scan rates, yielding a Cdl value of 4.02 mF cm^{-2}, which is higher than that of Pt/C (2.85 mF cm^{-2}). The larger Cdl indicates that Pt/Sn NSs expose more accessible electrochemically active sites, consistent with the uniform distribution of ultrasmall Pt nanoparticles observed by TEM. In addition, electrochemical impedance spectroscopy (EIS) measurements show that Pt/Sn NSs possess a smaller Nyquist semicircle than Pt/C in 0.5 M H_2SO_4 [Supplementary Figure 8], revealing lower charge-transfer resistance and faster interfacial electron transport[16,47]. Supplementary Figure 9 further shows only a 14 mV change in overpotential after 2,000 CV cycles, indicating favorable acidic cycling durability. More generally, interface engineering in supported HER catalysts has been shown to regulate active-site reactivity through metal-support coupling[48].

The alkaline HER performance was then evaluated in 1.0 M KOH. As illustrated in Figure 3D, Pt/Sn NSs exhibit markedly enhanced HER activity compared with commercial Pt/C, requiring overpotentials of only 37 and 114 mV to reach current densities of 10 and 100 mA cm^{-2}, respectively, compared with 49 and 220 mV for Pt/C. The corresponding overpotential comparison is presented in Figure 3E. The smaller overpotentials are particularly notable at high current density, where water adsorption and dissociation can strongly influence alkaline HER kinetics[49-51]. As shown in Figure 3F, the Pt/Sn NSs deliver a lower Tafel slope of 35.7 mV dec^{-1} compared to commercial Pt/C (65.2 mV dec^{-1}), indicating faster alkaline HER kinetics. The corresponding current-density fitting ranges and linear regression parameters are summarized in Supplementary Table 4, and the fitted-line coordinates for the alkaline electrolyte are provided in Supplementary Table 6. Because alkaline HER includes the additional water adsorption/dissociation process prior to H* formation, this kinetic improvement is consistent with the more efficient formation and conversion of H* intermediates[49-51]. These results are consistent with strong Pt-Sn interfacial electronic coupling and support-induced modulation of the Pt active sites.

The mass activities were evaluated at a geometric current density of 10 mA cm^{-2} in the respective electrolytes by normalizing the corresponding current to the mass of Pt loaded on each working electrode. As shown in Supplementary Figure 10, the Pt/Sn NSs exhibit a mass activity of 16.99 A $mgPt^{-1}$ in 1.0 M KOH, much higher than that of commercial Pt/C (6.05 A $mgPt^{-1}$). This result shows that the Pt nanoparticles anchored on Sn NSs possess higher Pt utilization efficiency. The enhanced mass activity can be attributed to the uniform dispersion of ultrasmall Pt nanoparticles on the two-dimensional Sn support and the abundant Pt-Sn interfacial sites, which allow more Pt atoms to effectively participate in the HER process. The intrinsic activity of the catalytic sites was further assessed by TOF analysis. As shown in Supplementary Figure 11, the Pt/Sn NSs show higher TOF values than commercial Pt/C over the tested overpotential range. At an overpotential of 45 mV, the TOF value of the Pt/Sn NSs reaches approximately 1.16 s^{-1}, which is much higher than that of Pt/C. The relative electrochemically accessible surface area was assessed using the double-layer capacitance obtained from CV measurements in the non-Faradaic region [Supplementary Figure 12]. As shown in Supplementary Figure 13, the Pt/Sn NSs show larger capacitive currents than Pt/C at different scan rates, giving a Cdl value of 5.06 mF cm^{-2}, greater than that of Pt/C (3.52 mF cm^{-2}). In addition, EIS measurements reveal that Pt/Sn NSs possess a much smaller Nyquist semicircle than Pt/C in 1.0 M KOH [Supplementary Figure 14], demonstrating a lower charge-transfer resistance and faster interfacial electron transport during alkaline HER. The durability of the Pt/Sn NSs was also evaluated under alkaline conditions. Supplementary Figure 15 shows that after 2,000 CV cycles, the polarization curve of the Pt/Sn NSs shows only a small negative shift of 16 mV, indicating good cycling stability in 1.0 M KOH.

To clarify the intrinsic contribution of the Sn nanosheet support, bare Sn NSs were introduced as an additional control catalyst. As shown in Supplementary Figure 16, the bare Sn NSs exhibit substantially lower HER activity than the Pt/Sn NSs under both acidic and alkaline conditions, demonstrating that the intrinsic activity of the bare Sn NSs alone cannot account for the enhanced HER performance. The pronounced activity enhancement is observed after Pt incorporation into the Pt/Sn architecture.

The reproducibility of the HER measurements was further verified using five independent linear sweep voltammetry (LSV) measurements. The repeated polarization curves and corresponding statistical analyses [mean ± standard deviation (SD), $n = 5$] for the Pt/Sn NSs, commercial Pt/C, and bare Sn NSs under acidic and alkaline conditions are provided in Supplementary Figures 17 and 18.

The HER performance of the Pt/Sn NSs was further compared with that of recently reported HER electrocatalysts. As summarized in Figure 3G and Supplementary Tables 2 and 3, the Pt/Sn NSs display competitive HER activity under both acidic and alkaline conditions[52-56].

Finally, the electrochemical durability of Pt/Sn NSs was evaluated via long-term chronoamperometric measurements under constant applied potentials. As shown in Figure 3H and Supplementary Figure 19, the Pt/Sn NSs maintain relatively stable current-density responses during continuous operation for 30 h in both 0.5 M H_2SO_4 and 1.0 M KOH, with only limited current attenuation observed throughout the test. These results demonstrate the satisfactory operational stability of the Pt/Sn NSs under both acidic and alkaline HER conditions. Furthermore, TEM, XRD, and XPS analyses were performed after 30 h of HER operation in 0.5 M H_2SO_4 [Supplementary Figure 20]. Nanosheet-like features remain visible in the examined TEM regions, the principal XRD reflections are retained, and Pt- and Sn-related signals remain detectable in the post-test XPS spectra. These observations support the retention of the main crystalline features and the presence of Pt and Sn at the surface after acidic HER operation.

Density functional theory calculations

Density functional theory (DFT) calculations were performed to further explore the electronic origin and HER reaction thermodynamics of the Pt/Sn NSs in both acidic and alkaline media. Representative structural models of Pt/Sn NSs and Pt/C were constructed, and the structural configurations of the corresponding intermediates during the acidic and alkaline HER processes are detailed in Supplementary Figures 21-24.

The binding energies between Pt species and the corresponding supports were calculated to evaluate the strength of the Pt-support interaction. As shown in Figure 4A, Pt/Sn NSs exhibit a binding energy of -8.64 eV, which is substantially more negative than that of Pt/C (-2.96 eV). This result indicates a markedly stronger Pt-support interaction with Sn nanosheets than with the conventional carbon support. The stronger interaction is consistent with the electronically active nature of Sn and suggests stronger coupling between Pt species and the Sn nanosheet support.

Charge-density-difference analysis was performed to examine the interfacial electronic redistribution. The cyan regions represent electron depletion, whereas the yellow regions indicate electron accumulation[11,12,28,29]. As shown in Figure 4B and C, pronounced electron accumulation is observed around Pt atoms in the Pt/Sn NSs together with electron depletion on the Sn nanosheet side, indicating directional charge redistribution from Sn toward Pt; by contrast, Pt/C exhibits much weaker charge redistribution. The plane-averaged charge-density-difference profiles [Supplementary Figures 25 and 26] and Bader charge analysis further support this trend, as the Pt cluster in the Pt/Sn NSs gains approximately 1.08 e from the Sn nanosheet support, whereas Pt in Pt/C slightly loses approximately 0.08 e to the carbon support [Supplementary Figure 27]. These results collectively support strong Pt-Sn interfacial electronic coupling and support-induced

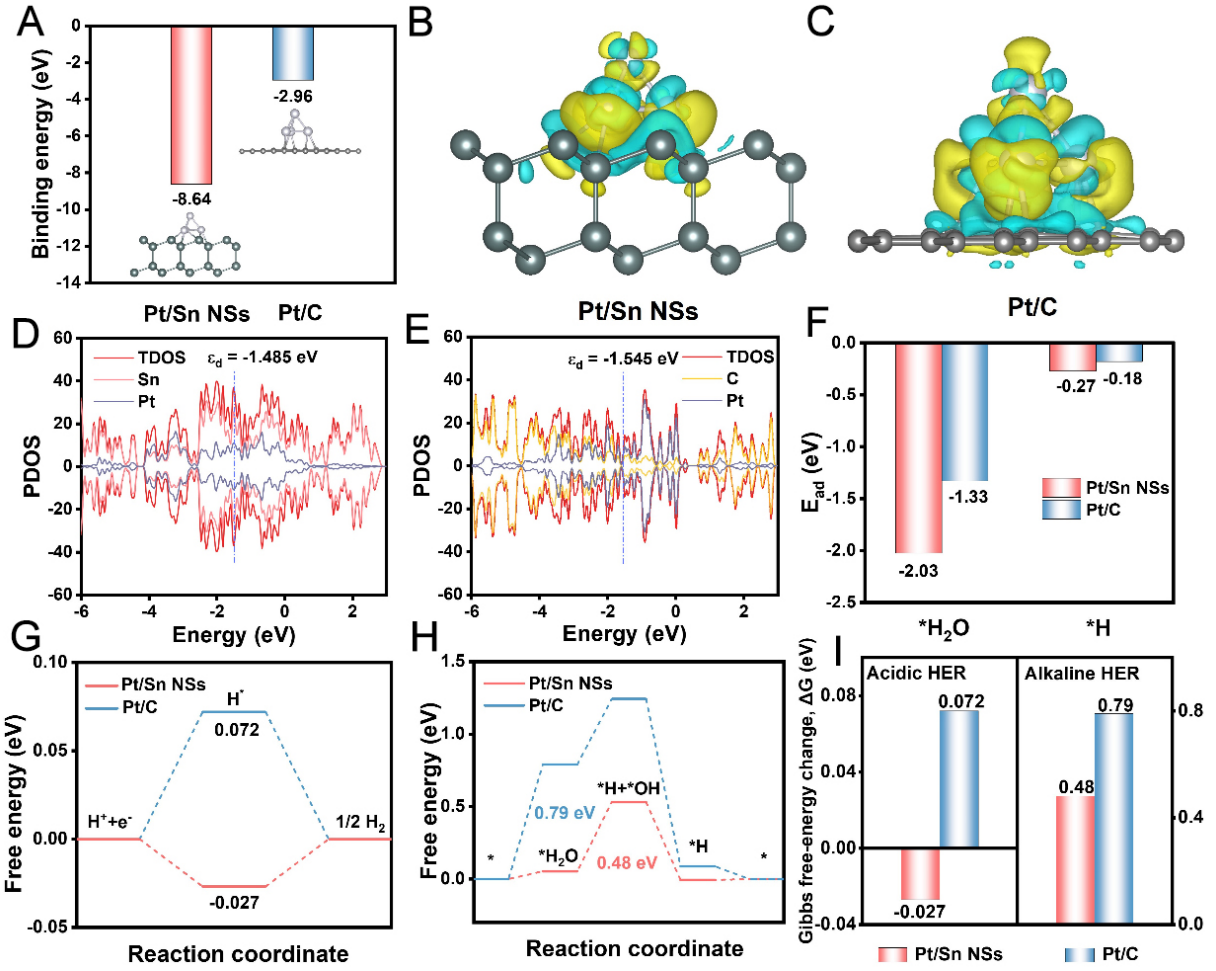


Figure 4. Theoretical investigation of the Pt-support interaction and HER reaction thermodynamics. (A) Calculated binding energies of Pt/Sn NSs (-8.64 eV) and Pt/C (-2.96 eV); the red and blue data series represent Pt/Sn NSs and Pt/C, respectively; (B and C) Charge-density-difference maps of the Pt/Sn NSs and Pt/C, respectively, in which the yellow and cyan regions indicate electron accumulation and electron depletion, respectively; (D and E) Calculated density of states and Pt d-band centers of the Pt/Sn NSs and Pt/C, respectively; the legends distinguish the total density of states (TDOS) and element-resolved projected density of states (PDOS); (F) Adsorption energies of H* and H_2O on the Pt/Sn NSs and Pt/C, where the red and blue bars represent Pt/Sn NSs and Pt/C, respectively; (G) Acidic and (H) alkaline HER free-energy diagrams comparing the Pt/Sn NSs with Pt/C; the red and blue curves represent Pt/Sn NSs and Pt/C, respectively; (I) Comparison of the Gibbs free-energy changes (ΔG) associated with key HER steps on Pt/Sn NSs and Pt/C under acidic and alkaline conditions. The red and blue bars represent Pt/Sn NSs and Pt/C, respectively, and the left and right y-axes correspond to the acidic and alkaline HER free-energy scales. For alkaline HER, the values represent the maximum uphill Gibbs free-energy changes between successive states along the pathways shown in (H): 0.79 eV for H_2O adsorption on Pt/C and 0.48 eV for H_2O dissociation on Pt/Sn NSs. The H* adsorption energies in (F) are electronic energies, whereas the Gibbs free energies in (G) include zero-point-energy and entropy corrections. Pt/Sn NSs: Pt nanoparticle-modified Sn nanosheets; HER: hydrogen evolution reaction; Pt/C: platinum-on-carbon.

modulation of the Pt electronic structure. The corresponding density-of-states analysis [Figure 4D and E] shows that the Pt d-band center in Pt/Sn NSs shifts upward toward the Fermi level relative to Pt/C. According to the d-band framework, this trend is consistent with a relative strengthening of Pt-adsorbate interaction; however, the catalytic consequence cannot be inferred from the d-band-center position alone and must be assessed together with the adsorption thermodynamics[57].

The adsorption energies of H_2O and H* were further examined [Figure 4F]. The calculated H_2O adsorption energies are -2.03 eV on Pt/Sn NSs and -1.33 eV on Pt/C, while the corresponding H* adsorption energies are -0.27 and -0.18 eV, respectively. These results indicate stronger adsorption of both H_2O and H* on Pt/Sn NSs, demonstrating that the Sn nanosheet support modulates the adsorption energetics at Pt sites.

The hydrogen adsorption free energies further clarify the influence of support-induced electronic modulation on HER thermodynamics. Pt/C exhibits a ΔG(H*) value of +0.072 eV, indicating slightly weak H* adsorption relative to the ideal thermoneutral condition, whereas Pt/Sn NSs exhibit a ΔG(H*) value of -0.027 eV. Thus, the Sn-induced electronic modulation moderately strengthens the Pt-H interaction while reducing the absolute deviation of ΔG(H*) from zero from 0.072 to 0.027 eV, providing a more nearly thermoneutral H* adsorption/desorption balance[58]. The Gibbs free-energy diagrams further illustrate the reaction thermodynamics under acidic and alkaline conditions [Figure 4G-I]. The energetics of water-involved steps are important for alkaline HER. Li *et al.* associated the reduced energy requirement of the Volmer step on Pt nanoparticles supported on nitrogen-sulfur co-doped carbon with facilitated water dissociation and H* formation[42]. In the present calculations, the maximum uphill Gibbs free-energy change between successive states along the alkaline HER pathway shown in Figure 4H is 0.48 eV for Pt/Sn NSs and 0.79 eV for Pt/C, corresponding to H_2O dissociation and H_2O adsorption, respectively. Together with the more nearly thermoneutral H* adsorption, the smaller maximum uphill free-energy change provides a thermodynamic basis for understanding the enhanced HER performance of Pt/Sn NSs. Accordingly, the d-band-center shift is treated as an electronic-structure descriptor rather than direct evidence that stronger H adsorption is intrinsically favorable, and the adsorption thermodynamics are assessed directly from the calculated ΔG values.

CONCLUSIONS

Pt nanoparticle-modified Sn nanosheets were developed as efficient HER electrocatalysts for both acidic and alkaline media through a liquid-phase exfoliation and ALD strategy. The two-dimensional Sn nanosheets provide abundant anchoring sites for the uniform nucleation of ultrasmall Pt nanoparticles and construct a well-defined 0D/2D Pt/Sn NSs heterostructure. Compared with conventional carbon supports, electronically active Sn nanosheets induce stronger Pt-support coupling and pronounced interfacial charge redistribution, as supported by XPS analyses and DFT calculations. This strengthened electronic interaction regulates the electronic structure of Pt active sites and contributes to the enhanced HER performance of the Pt/Sn NSs under both acidic and alkaline conditions, requiring only 28 and 37 mV to reach 10 mA cm^{-2} in 0.5 M H_2SO_4 and 1.0 M KOH, respectively. Theoretical calculations further show that support-induced electronic modulation brings H* adsorption closer to thermoneutrality and provides more favorable reaction thermodynamics for the key acidic and alkaline HER steps. These results establish two-dimensional Sn nanosheets as electronically active supports for regulating Pt-based HER catalysis.

DECLARATIONS

Authors' contributions

Original draft, investigation, data curation, formal analysis, methodology and conceptualization: Huang, Y.; Jiao, H.
Original draft, conceptualization, review and editing: Zhao, L.
Formal analysis and data curation: Yu, T.; Liu, L.
Conceptualization and supervision: Li, F.
Data curation and visualization: Zhao, M.; Bai, Q.; Wang, J.
Editing and supervision: Bai, B.; Li, J.
Review, supervision, formal analysis, conceptualization: Leng, X.

Availability of data and materials

The raw data supporting the findings of this study are available within this Article and its Supplementary Materials. Further data are available from the corresponding authors upon request.

AI and AI-assisted tools statement

Not applicable.

Financial support and sponsorship

This work was supported by Shenzhen Introduce High-level Talents and Scientific Research Start-up Funds (NA1140900125, NA1140904, QY1140901826), Guangdong Basic and Applied Basic Research Foundation (No. 2023A1515110901), Shenzhen Science and Technology Program (Grant No. RCBS20231211090700002), Fund Program for the Scientific Activities of Selected Returned Overseas Professionals in Shanxi Province (20250007), Key Research and Development Program for School-Local Cooperation in Lvliang City (2025XDHZ07), Basic Technological Research Project (JBGS2024-431-003), National Natural Science Foundation of China (No. 12605263).

Conflicts of interest

All authors declared that there are no conflicts of interest.

Ethical approval and consent to participate

Not applicable.

Consent for publication

Not applicable.

Copyright

© The Author(s) 2026.

Supplementary Materials

Supplementary Materials

REFERENCES

1. Roger, I.; Shipman, M. A.; Symes, M. D. Earth-abundant catalysts for electrochemical and photoelectrochemical water splitting. *Nat. Rev. Chem.* **2017**, *1*, 0003. DOI
2. Mahmood, J.; Li, F.; Jung, S.; et al. An efficient and pH-universal ruthenium-based catalyst for the hydrogen evolution reaction. *Nat. Nanotechnol.* **2017**, *12*, 441-6. DOI
3. Zheng, Y.; Jiao, Y.; Zhu, Y.; et al. Hydrogen evolution by a metal-free electrocatalyst. *Nat. Commun.* **2014**, *5*, 3783. DOI
4. Shi, Z.; Zhang, X.; Lin, X.; et al. Phase-dependent growth of Pt on MoS_2 for highly efficient H_2 evolution. *Nature* **2023**, *621*, 300-5. DOI
5. Guo, F.; Macdonald, T. J.; Sobrido, A. J.; Liu, L.; Feng, J.; He, G. Recent advances in ultralow-Pt-loading electrocatalysts for the efficient hydrogen evolution. *Adv. Sci.* **2023**, *10*, 2301098. DOI PubMed PMC
6. Zhao, Y.; Kumar, P. V.; Tan, X.; et al. Modulating Pt-O-Pt atomic clusters with isolated cobalt atoms for enhanced hydrogen evolution catalysis. *Nat. Commun.* **2022**, *13*, 2430. DOI PubMed PMC
7. Cheng, N.; Stambula, S.; Wang, D.; et al. Platinum single-atom and cluster catalysis of the hydrogen evolution reaction. *Nat. Commun.* **2016**, *7*, 13638. DOI PubMed PMC
8. Sui, X.; Zhang, L.; Li, J.; et al. Advanced support materials and interactions for atomically dispersed noble-metal catalysts: from support effects to design strategies. *Adv. Energy. Mater.* **2022**, *12*, 2102556. DOI
9. Kim, S.; Park, J.; Hwang, J.; Lee, J. Effects of functional supports on efficiency and stability of atomically dispersed noble-metal electrocatalysts. *EnergyChem* **2021**, *3*, 100054. DOI
10. Liu, Y.; Wang, Q.; Zhang, J.; et al. Recent advances in carbon-supported noble-metal electrocatalysts for hydrogen evolution reaction: syntheses, structures, and properties. *Adv. Energy. Mater.* **2022**, *12*, 2200928. DOI
11. Shi, Y.; Ma, Z.; Xiao, Y.; et al. Electronic metal-support interaction modulates single-atom platinum catalysis for hydrogen evolution reaction. *Nat. Commun.* **2021**, *12*, 3021. DOI
12. Harsha, S.; Sharma, R. K.; Dierner, M.; et al. Dewetting of Pt nanoparticles boosts electrocatalytic hydrogen evolution due to electronic metal-support interaction. *Adv. Funct. Mater.* **2024**, *34*, 2403628. DOI
13. Yu, W.; Huang, H.; Qin, Y.; et al. The synergistic effect of pyrrolic-N and pyridinic-N with Pt under strong metal-support interaction to achieve high-performance alkaline hydrogen evolution. *Adv. Energy. Mater.* **2022**, *12*, 2200110. DOI
14. Wu, X.; Wang, Z.; Zhang, D.; et al. Solvent-free microwave synthesis of ultra-small Ru-Mo_2C@CNT with strong metal-support interaction for industrial hydrogen evolution. *Nat. Commun.* **2021**, *12*, 4018. DOI PubMed PMC
15. Feng, Y.; Xie, Y.; Yu, Y.; et al. Electronic metal-support interaction induces hydrogen spillover and platinum utilization in hydrogen evolution reaction. *Angew. Chem. Int. Ed.* **2025**, *64*, e202413417. DOI

16. Smiljanić, M.; Panić, S.; Bele, M.; et al. Improving the HER activity and stability of Pt nanoparticles by titanium oxynitride support. *ACS. Catal.* **2022**, *12*, 13021-33. DOI PubMed PMC
17. Poudel, M. B.; Logeshwaran, N.; Prabhakaran, S.; Kim, A. R.; Kim, D. H.; Yoo, D. J. Low-cost hydrogen production from alkaline/seawater over a single-step synthesis of Mo_3Se_4-NiSe core-shell nanowire arrays. *Adv. Mater.* **2024**, *36*, 2305813. DOI
18. Liu, Y.; Chen, Y.; Tian, Y.; et al. Synergizing hydrogen spillover and deprotonation by the internal polarization field in a MoS_2/$NiPS_3$ vertical heterostructure for boosted water electrolysis. *Adv. Mater.* **2022**, *34*, 2203615. DOI
19. Bu, X.; Bu, Y.; Quan, Q.; et al. Superior electrocatalyst for all-pH hydrogen evolution reaction: heterogeneous Rh/N and S co-doped carbon yolk-shell nanospheres. *Adv. Funct. Mater.* **2022**, *32*, 2206006. DOI
20. Zhang, Y.; Yu, W.; Zhang, H.; et al. The superaerophobic N-doped carbon nanocage with hydrogen spillover effort for enhanced hydrogen evolution. *Small* **2024**, *20*, 2308440. DOI
21. Wang, Z.; Liu, R.; Sun, T.; et al. Revealing hydrogen spillover on 1T/2H MoS_2 heterostructures for an enhanced hydrogen evolution reaction by scanning electrochemical microscopy. *Anal. Chem.* **2024**, *96*, 7618-25. DOI
22. Xie, L.; Wang, L.; Liu, X.; et al. Flexible tungsten disulfide superstructure engineering for efficient alkaline hydrogen evolution in anion exchange membrane water electrolysers. *Nat. Commun.* **2024**, *15*, 5702. DOI PubMed PMC
23. Shen, J.; Chen, C.; Wei, Z.; et al. Ru nanoclusters embedded by amorphous NiP alloy with strong metal-support interaction for durable and efficient industrial alkaline water electrolysis. *Appl. Catal. B. Environ. Energy.* **2026**, *385*, 126301. DOI
24. Li, L.; Tian, F.; Wu, F.; et al. Strong electronic metal-support interaction of Ni_4Mo/N-$SrMoO_4$ promotes alkaline hydrogen electrocatalysis. *Appl. Catal. B. Environ. Energy.* **2025**, *361*, 124660. DOI
25. Xiao, Z.; Yang, M.; Wang, J.; et al. FeNiP/MoO_x integrated electrode grown on monocrystalline $NiMoO_4$ nanorods with multi-interface for accelerating alkaline hydrogen evolution reaction. *Appl. Catal. B. Environ.* **2022**, *303*, 120913. DOI
26. Gerber, I. C.; Serp, P. A theory/experience description of support effects in carbon-supported catalysts. *Chem. Rev.* **2020**, *120*, 1250-349. DOI PubMed
27. Rong, H.; Ji, S.; Zhang, J.; Wang, D.; Li, Y. Synthetic strategies of supported atomic clusters for heterogeneous catalysis. *Nat. Commun.* **2020**, *11*, 5884. DOI PubMed PMC
28. Zhou, C.; Ma, K.; Zhuang, Z.; et al. Tuning the local environment of Pt species at CNT@MO_{2-x} (M = Sn and Ce) heterointerfaces for boosted alkaline hydrogen evolution. *J. Am. Chem. Soc.* **2024**, *146*, 21453-65. DOI
29. Yan, Q.; Wu, D.; Chu, S.; et al. Reversing the charge transfer between platinum and sulfur-doped carbon support for electrocatalytic hydrogen evolution. *Nat. Commun.* **2019**, *10*, 4977. DOI PubMed PMC
30. Lu, Z.; Wang, J.; Zhang, P.; et al. Directed electron transport induced surface reconstruction of 2D NiFe-LDH/Stanene heterojunction catalysts for efficient oxygen evolution. *Appl. Catal. B. Environ. Energy.* **2024**, *353*, 124073. DOI
31. Pauling, L. The nature of the chemical bond. IV. The energy of single bonds and the relative electronegativity of atoms. *J. Am. Chem. Soc.* **1932**, *54*, 3570-82. DOI
32. Wu, Z.; Yang, P.; Li, Q.; et al. Microwave synthesis of Pt clusters on black TiO_2 with abundant oxygen vacancies for efficient acidic electrocatalytic hydrogen evolution. *Angew. Chem. Int. Ed.* **2023**, *62*, e202300406. DOI
33. Weng, G.; Alexandrova, A. N. Unraveling the surface termination and evolution of surface states for electrocatalyst $PtSn_4$ in alkaline HER. *ACS. Catal.* **2025**, *15*, 10448-58. DOI
34. Yu, Y.; Wang, Q.; Li, X.; et al. Laser-thermal reduction synthesis of high-entropy alloys towards high-performance pH universal hydrogen evolution reaction. *Nano. Mater. Sci.* **2025**, *7*, 400-8. DOI
35. Dai, C.; Wang, R.; Yao, S.; et al. Cobalt nanoclusters-modulated platinum-tin intermetallic for pH-universal hydrogen evolution electrocatalysis. *ACS. Mater. Lett.* **2025**, *7*, 1760-7. DOI
36. Huang, R.; Huang, Z.; Zhao, P.; et al. Unveiling the formation mechanisms of the Pt-Sn intermetallic phase within Pt-SnO_2 for the enhanced hydrogen evolution reaction. *ACS. Nano.* **2026**, *20*, 7886-97. DOI
37. Dendooven, J.; Ramachandran, R. K.; Solano, E.; et al. Independent tuning of size and coverage of supported Pt nanoparticles using atomic layer deposition. *Nat. Commun.* **2017**, *8*, 1074. DOI PubMed PMC
38. Zhang, B.; Chen, S.; Wulan, B.; Zhang, J. Surface modification of SnO_2 nanosheets via ultrathin N-doped carbon layers for improving CO_2 electrocatalytic reduction. *Chem. Eng. J.* **2021**, *421*, 130003. DOI
39. Yuan, D.; Hu, Z.; Chen, Z.; et al. Atomic-level Tailoring of the electronic metal-support interaction between Pt-Co_3O_4 interfaces for high hydrogen evolution performance. *J. Phys. Chem. Lett.* **2024**, *15*, 3486-92. DOI
40. Rui, K.; Zhao, G.; Lao, M.; et al. Direct hybridization of noble metal nanostructures on 2D metal-organic framework nanosheets to catalyze hydrogen evolution. *Nano. Lett.* **2019**, *19*, 8447-53. DOI

41. Han, X.; Wu, X.; Deng, Y.; et al. Ultrafine Pt nanoparticle-decorated pyrite-type CoS_2 nanosheet arrays coated on carbon cloth as a bifunctional electrode for overall water splitting. *Adv. Energy. Mater.* **2018**, *8*, 1800935. DOI
42. Li, Y.; Luo, J.; Liu, P.; et al. Sulfur doping activated metal-support interaction drives Pt nanoparticles to achieve acid-base hydrogen evolution reaction. *J. Mater. Chem. A.* **2025**, *13*, 11518-29. DOI
43. Liu, X.; Zhou, Y.; Lin, J.; et al. Directional growth and density modulation of single-atom platinum for efficient electrocatalytic hydrogen evolution. *Angew. Chem. Int. Ed.* **2024**, *63*, e202406650. DOI
44. Wan, C.; Ling, Y.; Wang, S.; Pu, H.; Huang, Y.; Duan, X. Unraveling and resolving the inconsistencies in tafel analysis for hydrogen evolution reactions. *ACS. Cent. Sci.* **2024**, *10*, 658-65. DOI PubMed PMC
45. Li, J.; Liu, H.; Gou, W.; et al. Ethylene-glycol ligand environment facilitates highly efficient hydrogen evolution of Pt/CoP through proton concentration and hydrogen spillover. *Energy. Environ. Sci.* **2019**, *12*, 2298-304. DOI
46. Zhou, Y.; Liu, X.; Yu, C.; et al. Boosting hydrogen evolution through hydrogen spillover promoted by Co-based support effect. *J. Mater. Chem. A.* **2023**, *11*, 6945-51. DOI
47. Li, Q.; Chen, C.; Luo, W.; et al. In situ active site refreshing of electro-catalytic materials for ultra-durable hydrogen evolution at elevated current density. *Adv. Energy. Mater.* **2024**, *14*, 2304099. DOI
48. Gao, T.; Tang, X.; Li, X.; et al. Understanding the atomic and defective interface effect on ruthenium clusters for the hydrogen evolution reaction. *ACS. Catal.* **2023**, *13*, 49-59. DOI
49. Luo, J.; Sun, Y.; Liu, P.; et al. Nitrogen-containing-defect-site-assisted H_2O adsorption and dissociation on crystalline Ru nanoclusters by quasi-hydrogen bonds boosts alkaline hydrogen evolution reaction. *ACS. Sustainable. Chem. Eng.* **2024**, *12*, 5319-31. DOI
50. Subbaraman, R.; Tripkovic, D.; Strmcnik, D.; et al. Enhancing hydrogen evolution activity in water splitting by tailoring Li^+-$Ni(OH)_2$-Pt interfaces. *Science* **2011**, *334*, 1256-60. DOI
51. Zhou, K. L.; Wang, Z.; Han, C. B.; et al. Platinum single-atom catalyst coupled with transition metal/metal oxide heterostructure for accelerating alkaline hydrogen evolution reaction. *Nat. Commun.* **2021**, *12*, 3783. DOI PubMed PMC
52. Jia, H.; Wang, H.; Yan, F.; Zhang, H.; Li, Z.; Wang, J. Unravelling electrocatalytic concerted diatomic-ensembles over superior hydrogen-evolution array structured by NiMo/Mo_2N heteronanojunctions. *Appl. Catal. B. Environ.* **2024**, *343*, 123362. DOI
53. Wang, Z.; Xiao, B.; Lin, Z.; et al. $PtSe_2$/Pt heterointerface with reduced coordination for boosted hydrogen evolution reaction. *Angew. Chem. Int. Ed.* **2021**, *60*, 23388-93. DOI
54. Dong, Y.; Deng, Z.; Zhang, H.; Liu, G.; Wang, X. A highly active and durable hierarchical electrocatalyst for large-current-density water splitting. *Nano. Lett.* **2023**, *23*, 9087-95. DOI
55. Zhang, B.; Wang, J.; Liu, G.; et al. A strongly coupled Ru-CrO_x cluster-cluster heterostructure for efficient alkaline hydrogen electrocatalysis. *Nat. Catal.* **2024**, *7*, 441-51. DOI
56. Pu, Z.; Amiinu, I. S.; Kou, Z.; Li, W.; Mu, S. RuP_2-based catalysts with platinum-like activity and higher durability for the hydrogen evolution reaction at all pH values. *Angew. Chem. Int. Ed.* **2017**, *56*, 11559-64. DOI PubMed
57. Hammer, B.; Nørskov, J. Electronic factors determining the reactivity of metal surfaces. *Surf. Sci.* **1995**, *343*, 211-20. DOI
58. Nørskov, J. K.; Bligaard, T.; Logadottir, A.; et al. Trends in the exchange current for hydrogen evolution. *J. Electrochem. Soc.* **2005**, *152*, J23. DOI

Disclaimer/Publisher's Note: All statements, opinions, and data contained in this publication are solely those of the individual author(s) and contributor(s) and do not necessarily reflect those of OAE and/or the editor(s). OAE and/or the editor(s) disclaim any responsibility for harm to persons or property resulting from the use of any ideas, methods, instructions, or products mentioned in the content.

© The Author(s) 2026. Open Access This article is licensed under a Creative Commons Attribution 4.0 International License (https://creativecommons.org/licenses/by/4.0/), which permits unrestricted use, sharing, adaptation, distribution and reproduction in any medium or format, for any purpose, even commercially, as long as you give appropriate credit to the original author(s) and the source, provide a link to the Creative Commons license, and indicate if changes were made.